Self-powered smart skins for multimodal tactile perception based on triboelectric and hygroelectric working principles

Xiaoting Ma[1], Eunjong Kim[1], Jiaming Zhou[1], Jingyi Gao[1], Chuntae Kim[2], Xiao Huan[1], Ji Tae Kim[1], Dong-Myeong Shin[1,*]

[1] Department of Mechanical Engineering, The University of Hong Kong, Pokfulam Road, Hong Kong, China
[2] Bionanotechnology Research Center, Korea Research Institute of Bioscience and Biotechnology (KRIBB), Daejeon, 34141, Republic of Korea

* E-mail: dmshin@hku.hk

Abstract

Human being perceives multiple tactile modalities in the process of sensation on the skin and interpretation in the brain. To date, several sensing techniques facilitate the accurate measurement of individual tactile modality, but multimodal static and dynamic sensing remain challenging. Moreover, low-cost and highly efficient interpretation techniques are still required for tactile perception. Herein, we present cost-effective and high-performing self-powered smart skins that mimic multimodal tactile perception, enabling accurate perception of pressure, vibration, and humidity in the process of sensation on the smart skin and interpretation by machine learning. The dynamic and static stimuli are encoded by triboelectric and hygroelectric principles in the smart skins, respectively, while the hygroscopic nature empowers humidity sensation capability in the

smart skin with an accuracy rate as high as 84.0%-100.0%. We believe our smart skin will enable the smooth transition of e-skin into practical applications, such as robotics, prosthetics, healthcare, and intelligent industry.

Keywords: smart skins, multimodal tactile perception, self-powred sensor, triboelectric sensor, hygroelectric sensor

Introduction

Human skin plays an essential role in tactile sensation in direct contact with the external environment as an integumentary layer of the body. Tactile modalities, such as pressure, vibration, warm, cold, and humidity, activate the subcutaneous sensory receptors, offering electrical signals for further identification and interpretation of the stimuli information at the somatosensory cortex[1]. The mechanoreceptors perceive pressure and vibration while thermoreceptors encode thermal stimuli. In particular, the humidity can be detected by thermoreceptors in tandem with mechanoreceptors in the human skin due to the absence of hygroreceptors[2]. Increasing demand in sectors including robotics[3-5], prosthetics[6] , and healthcare[7, 8] is triggering research into tactile sensors that feature sensitivity to pressure[9, 10], temperature[11], and humidity[12]. Some efforts have been successfully made to mimic the static tactile sensation based on the various working principles of piezoresistive[13, 14], piezoelectric[15, 16], capacitive[13, 17], and pyroelectric[18, 19] . However, the slow response rate of functional materials has hindered the fast response to dynamic stimuli[20, 21]. Further, as perception includes processes of not only tactile sensing on the skin but also identification and interpretation in the brain, it remains challenging to imitate the tactile perception of the human being exactly. Although the analytic software consciously coded has shown to perform well for identification and interpretation, it still requires sophisticated data acquisition and processing algorithms. Hence, there is a need for a smart tactile perception system in the range of detection to interpretation, including but not limited to organization, identification, and prediction in a manner of low-cost and high efficiency.

Triboelectric nanogenerators (TENGs) have been successfully put forward for encryption technology of the mechanical to the electrical domain in the broad range of stimuli frequency, being demonstrated as energy harvesters[22-26] and sensors[27-30]. The TENGs can be served as a

powerful tool to effectively sense the dynamic tactile sensation since they provide many advantages, such as simple fabrication, simple device structure, lightweight, fast response time and high energy conversion efficiency[31, 32]. On the other hand, the working mechanism of contact electrification and electrostatic induction inherently limits the sensitivity to static tactile sensation. In this regard, we designed and demonstrated cost-effective and high-performing smart skins that mimicked multimodal tactile perception based on triboelectricity principles in tandem with hygroelectricity. The key features mimicked for tactile perception are both static and dynamic responses of the sensing module, signal transmission, and data processing in the range of stimuli to perception. We found that the integration of the hygroscopic contact electrification layer into TENGs rendered the triboelectric smart skins module static stimuli sensitive in addition to the dynamic stimuli. Besides, the functional contact electrification layer endowed the moisture sensitivity to smart skins module for humidity sensing. The encoded signal measured by smart skins module was wirelessly transmitted to a central computer, and interpreted in the central computer with supervised machine learning. The smart skin system is shown to transcend the human sensory system in terms of quantitative pressure, vibration, and humidity perception, providing a new paradigm for a self-powered multimodal smart skin featuring low cost and high efficiency.

Results and discussion

Concept and design of a tactile perception smart finger

Humans percept environmental stimuli in conjunction with the somatosensory system in which mechano- and thermo-receptors in the skin encode the stimuli into electrical signals and the electrical signals are then evaluated in the sensory cortex (**Figure 1**a). In particular, the dynamic pressure and vibration (10 to 800 Hz) activate the fast-adapting (FA) mechanoreceptors while the

slow-adapting (SA) mechanoreceptors respond to the static pressure (0.1 to 100 kPa)[33-35]. The humidity is perceived by mechanoreceptors complexed with thermoreceptors due in large part to the absence of hygroreceptors in the human somatosensory system[2, 36]. Inspired by the human somatosensory system, we designed a tactile smart finger for pressure, vibration, and humidity perception based on triboelectricity and hygroelectricity, surpassing human tactile perception with regard to quantitative pressure, vibration, and humidity perception (Figure 1b). The smart finger is structurally composed of three layers: a single-ion conducting electrolyte, which serves as contact electrification as well as a hygroscopic layer, a gold electrode as an electrode, and a separatable aluminum electrode as a counter triboelectrification layer and electrode. Upon applying a periodic force of compressing and releasing to the Al electrode, the smart finger yields the instantaneous voltage outputs arising from the contact electrification between the electrolyte and the Al electrode, allowing it to mimic the FA receptors. The SA receptors are emulated by the steady voltage outputs generated by ion diffusion throughout the electrolyte sandwiched between asymmetric electrodes in the presence of contact. Furthermore, the pendant sulfonate anionic groups empower a hygroscopic nature into the electrolyte and the moisture uptake therefore determines the ion conduction in the electrolyte, rendering smart finger the humidity sensitive. The triboelectric (TE) and hygroelectric (HE) signals from the smart finger are recorded by smartphone, and the signals are transmitted to the main server computer for interpretation with the help of machine learning, imitating the peripheral and central nervous systems.

Pressure, vibration, and humidity sensation using smart finger

The smart finger was exposed to the course of a contacting, a pressing (4.9 kPa), and a releasing in the presence of 50 % relative humidity (RH) and analyzed to investigate the triboelectric and hygroelectric responses (**Figure 2**a). The electrical outputs exhibit distinct instantaneous peaks of

0.9 and –3.4 V while contacting and releasing, respectively, and the stable voltage of 81 mV has been found under continuous pressing. The primary principle of the smart finger can be rationalized through the transient electron flow arising from the humidity-sensitive ion diffusion and contact-electrification of the electrolytes throughout the pressing, the releasing, and the contacting (Figure 2b). In moderate humidity, the hygroscopic nature of the anionic electrolyte gives rise to moisture uptake, facilitating ion dissociation in the solid-state electrolyte, and thereby the concentration gradient of mobile charge across the electrolyte is formed by the asymmetric accessibility of moisture[37, 38]. The mobile charge diffusion in the electrolyte produces a continuous electron flow through the external circuit upon pressing the smart finger (Figure 2b(i), corresponding to contact HE signal in Figure 2a). The contact electrification at the interface between the electrolyte and the separatable electrode engenders the surface charges, driving the development of the electric field at the interface, and resultingly yielding a transient electron flow and an instantaneous voltage peak under the separation(Figure 2b(ii), corresponding to separation TE in Figure 2a). While approaching the separatable electrode to the electrolyte again, the electrons return back to the original electrode due to the fade of the electric field, resulting in the instantaneous voltage peak with reverse polarity (Figure 2b(iv), corresponding to contact TE in Figure 2a).

The sensitivity of hygroelectric signal was investigated in the presence of differing static pressure on the smart finger at the RH of 70% (Supplementary Figure 1), comparable to the typical human pressure perception range[17, 39]. The output voltage increased linearly with a sensitivity of 25 mV/kPa (Figure 2c), which we attribute to the greater tendency of interfacial resistance on decreased static pressure (Supplementary Figure 2). Under low static pressure, the weak interfacial contact impedes the charge recombination between proton and electrons at the interface, screening

the potential developed by the hygroelectricity. When increasing the static pressure, the greater contact results in less potential loss at the interface. The limit of detection was approximated by LoD = 3σ / S where σ is the standard deviation and S is sensitivity, and the LoD was accordingly determined to be 1.04 kPa, indicating that a small weight (0.1 N) on an area of 1 cm^2 can be detectable. The response time was confirmed to be approximately 5.3 and 5.1 ms for sensation and restoration, respectively (Supplementary Figure 3), denoting the vibration detection limit of up to ~200 Hz. This trait successfully affords biomimetic slow-adapting mechanoreceptors given that the frequency range of human vibration perception by slow-adapting receptors (Merkel cell) is shown to be <100 Hz[34]. Further, we analyzed the positive and negative triboelectric signals upon applying the dynamic pressure from 2.45 to 12.25 kPa (Supplementary Figure 4). As the effective area for contact electrification increases with dynamic pressure, the magnitude of negative outputs gradually becomes greater with increasing pressure, increasing up to 2.64 V under the 12.25 kPa. In contrast, the outputs of positive peaks remained stable regardless of the pressure applied (V_{PTE} = ~1 V). The triboelectric charges for contact and separation were calculated from the integration of a single current peak (Supplementary Figure 5), representing that the charge accounted for separation increases with humidity while the contact charge remains same. This trait is likely due to the fact that mobile cations in the electrolyte migrate from the surface to the stationary electrodes, so that the surface becomes more negative as increasing the humidity. When sufficient time is given for ion diffusion while being released state of the device, the surface charges are dissipated by the mobile charges returning to the original positions, bringing the constant contact charge in the process. We prepared the devices featuring anion-conducting, binary ion-conducting, and cation-conducting electrolytes in differing relative humidity. Remarkably, the output voltages of positive peaks are nearly stable for all marinated polymer electrolytes throughout the humidity

range (Figure 2d and Supplementary Figure 6), indicating that the charges developed on the polymer surfaces are independent of the humidity. For comparison, the polymer electrolyte was evaluated in the absence of mobile ions, acting as a typical dielectric triboelectrification layer. Its positive voltage peaks substantially decreased with increasing humidity as the moisture facilitates surface charge dissipation[40, 41]. In contrast, either anions or cations in the marinated polymers are expected to be mobile, giving rise to the compensation for the surface charge while the devices are separated, resulting in the constant surface charges remaining regardless of pressure and humidity.

We investigated the triboelectric output voltages under dynamic pressure of 4.9 kPa with variable frequency at the RH of 70% (Figure 2e and Supplementary Figure 7). The separation voltage peak of 1.2 V was achieved at an initial low frequency of 0.1 Hz, and the values were increased to 2.5 V in the frequency ranges of 0.3 to 1.1 Hz, in which frequency range we chose is crucial for smart finger applications like detecting heartbeats, feeling textures, and gripping objects. We attribute this frequency dependence to the insufficient relaxation of surface charge[24, 42], leading to surface charge accumulation upon repeated contact. Hence, a shorter relaxation time results in more significant charge accumulation at a higher frequency, demonstrating increased output voltage. Beyond the pressure and frequency sensitivity, the hygroscopic nature of the single-ion conducting electrolyte confers the humidity sensitivity on the smart finger, as presented in Figure 2f and Supplementary Figure 8. The measured output of hygroelectricity gradually increased with increasing the RH from 10 % to 80 %, reaching 0.97 V at the RH of 80 %. The single-ion conducting electrolyte has been shown to get heavy with humidifying the surrounding (Supplementary Figure 9) due largely to the moisture uptake. Polar solvating water facilitates ion dissociation and migration in a solid electrolyte[43, 44], and indeed the ion transport was found to be

fast with increasing the RH (Supplementary Figure 10), helping to rationalize the observed humidity sensitivity of the smart finger.

Self-powered smart finger for tactile perception

Ultimately, the different sensitivities to multiple stimuli, including pressure, vibration, and humidity, render this smart finger a promising platform for tactile perception by characterizing individual behaviors (Supplementary Figure 11). We first demonstrated the self-powering capabilities of the smart finger, and the power curves obtained from the different humidities are shown in **Figure 3**a and Supplementary Figure 12. The maximum powers generated in RH 10 and 80 % were 305 nW (at the load of 50 MΩ) and 25 nW (at the load of 20 MΩ), respectively, which stably charge the capacitor of 10 μF up to 2.3 and 0.97 V within 500 seconds at RH 10 and 80%, respectively (Figure 3b). It is worth noting that the electrical power generated at RH 10% mainly arises from triboelectricity, whereas hygroelectricity is the main contributor to yielding the power at RH 80 %, suggesting that energy delivery from either triboelectricity or hygroelectricity is large enough for self-powered smart finger operation. Furthermore, we successfully lit up a light-emitting diode (LED) under the reverse connection while the forward connection produced no noticeable light (Figure 3c), revealing that we can extract the separation TE peak from the single cycled electric signal using the LED lighting. The snapshots of the green LED with respect to different RHs, frequencies, and pressure are presented in Figure 3d and Supplementary Figure 13a. Slow vibration, high humidity and low pressure resulted in reduced brightness, and an increase in the vibration and pressure, and dry environment boosted brightness. To gain further in sight into the quantitative brightness of LEDs, we employed a home-built image analysis application in which the 8-bit RGB color components are extracted from the photographs taken by the mobile phone (Supplementary Figure 14 and Supplementary Movie 1). The perceived brightness (PB) was

approximated by the equation $PB = \sqrt{0.299\,R^2 + 0.587\,G^2 + 0.114\,B^2}$ [45] where R, G, B denote the values of RGB color components in 0 to 255 scales, respectively. The LED images in Figure 3d and Supplementary Figure 13a are converted into the brightness matrix, as plotted in Figure 3e and Supplementary Figure 13b, showing that the PB values correlated to each LED luminescent. Moreover, the PB values displayed a high degree of correlation (r^2 = 88.4 %) with 95 % confidence interval to the separation TE peaks (Figure 3f), which together imply that the separation TE signal of smart finger can be successfully elicited from the electrical signal using the PB of green LEDs reversely connected.

Implementing machine learning for tactile perception

Machine learning has been a well-established tool for building the model from sample data without being explicitly programmed, facilitating the prediction of a new data behavior comprising multidimensional features[46, 47]. Herein, the multiple features, including the contact TE, contact HE, separation TE, pressure, frequency, and humidity, were chosen for feature extraction in the machine learning algorithm. To identify the categorization of multiple features, we first aim to reduce high-dimensional data into two-dimensional space using linear discriminant analysis (LDA) in which the distance between each data in the category is minimized while the category distance is maximized. As shown in Figure 3g, we could clearly discriminate between a complex of humid, pressure, and vibrational conditions; low RH and vibrational conditions inclined to group together in the negative side of the first and second discriminant factors, respectively. Also, low pressure tended to cluster on the negative side of the first discriminant factor, whereas on the positive side of the second factor. The first two discriminant factors account for 99.8% of the variance. The confusion matrices of 8 humid, 9 pressure, and 6 vibrational conditions are presented in Figures 3h, 3i, and 3j, respectively, and high prediction accuracy was achieved for all matrices. Overall,

data clustering demonstrates discrimination capability and high reproducibility, putting forward potential applications of smart fingers for accurate sensing of pressure, vibration, and humidity.

On the basis of the pressure, vibration, and humidity discrimination capability of smart fingers outlined above, we demonstrated the real-world tactile perception of smart fingers incorporating machine learning for pressure, vibration, and humidity sensing. Figure 3k describes a flowchart detailing the tactile perception using smart fingers with the help of home built image analysis application and machine learning. First, the pre-trained model was developed using the collected data of known conditions in order to save calculation time and memory space for machine learning in a central computer. The dataset was preprocessed to label the feature matrix and split into training (80%) and test (20%) sets. With the linear regression algorithm based on a supervised machine learning, the relationship between dependent and independent features was successfully trained and was validified by the test dataset. The regression plot shown in Figure 3l exhibits the high accuracy of the pre-trained model with a high degree of correlation (r^2 = 99.3 %). Next, the smart finger acquires the contact HE and separation TE signals using a smart transmission handheld device (that is smartphone) in terms of perceived brightness and output voltage, and the signals are then transmitted to the central computer via wifi for perception in the pre-trained model (Supplementary Movie 2). The perception results are set to be simultaneously displayed on the screens of both the central computer and the handheld device (Supplementary Movie 3). Four conditions were chosen to test the perception accuracy of the smart finger, and the recognition results are presented in Supplementary Table 1.

Tactile perception mapping with multiarray smart skin

Beyond the tactile perception of the localized region, the multiarray of smart skin comprising 25 pixels of aluminum electrodes, Nafion electrolytes, and gold electrodes was constructed to

investigate the tactile perception performance of smart skin in line with spatial regions (Figure 4a). The electrode arrays were fabricated by a masked thermal evaporation technique. A 5 by 5 electrode array pattern was first defined on the paper mask, and the 100-nm-thick gold or aluminum films were then deposited on the polyethylene terephthalate (PET) substrate covered by stainless steel mask using a thermal evaporator. The Nafion electrolyte was punched into a 10 mm circular shape, and then placed on the gold electrode. The multiarray smart skin was obtained by covering the electrolyte with an aluminum electrode pattern on PET substrate. The polydimethylsiloxane (PDMS) spacers were located on the electrode substrate to secure a defined gap between electrolyte and aluminum electrode. The photographic images of a fabricated smart finger array presented in Figures 4b and 4c show the semi-transparency and high flexibility of our device, suggesting potential applications such as wearable electronic skins and biomedical sensors. The long-term stability was performed over the course of the 5000 compression-release cycles, as shown in Figure 4d, appearing to be stable compared with its initial voltage level. Insets of Figure 4d demonstrate the outstanding durability and robustness of smart fingers, revealed by scanning electron microscopy. The voltage signals of the nearest pixels (1,2,4, and 5) were investigated when the center pixel (3) was subjected to compression (Figure 4e), and a little crosstalk between adjacent pixels has been found. We note that the triboelectric signals have been observed for some adjacent pixels (1 and 5), which is likely attributed to the electrolyte-electrode distance change in the nearest pixels during compression. Response and relaxation time of approximately 150 ms were measured from the enlarged plots in Figure 4e. It is worthnoting that the multiarray smart skin exhibited the slower response time. We attribute the slower responses to the viscoelasticity of polymeric PET substrate, bringing the smart skin to be slowly deformed and recovered over the course of pressing and releasing[48, 49]. Lastly, the convex character patterns of ‘HKU’ was directly

pressured on the smart skin to demonstrate a 2-dimensional mapping of spatial stress (Supplementary Figure 15), and the resultant contact HE signals of the device at applied RHs of 30, 50, 70 % under the compressive force of 19.6 N were recorded using multichannel oscilloscope (Figure 4f and Supplementary Figure 16–18). The mapping images unambiguously present 'HKU' characters and the characters became more apparent at the elevated RHs, holding a promise for potential applications of our smart skin array as electronic skin. It is worth mentioning that our smart skin can be easily scaled–up or –down due in large part to its simple device architecture, indicating further room for resolution improvement down to 50 μm with the aid of the photolithographic technique.

Conclusion

We proposed a route to imitate multimodal human tactile perception from sensation to interpretation on the basis of triboelectric/hygroelectric sensing and machine learning algorithm. The contact electrification of the single-ion conducting electrolyte and separatable electrode facilitates the dynamic mechanical stimuli sensing, while the ion migration throughout the electrolyte enables the static sensing. Further, the hygroscopic nature of electrolytes endows the capability of humidity sensing. The smart skin comprising the single-ion conducting electrolyte and two electrodes converted static/dynamic mechanical stimuli and humidity into electrical signals. The encoded signals of smart skin were successfully interpreted into RHs, pressure, and vibration with an accuracy of 84.0 − 100.0% using the handheld device and machine learning, demonstrating a tactile perception of both local and spatial sensations. Our smart skin provides multiple advantages, including a simple fabrication, compact size, fast response, high accuracy, self-powering, and multimodal sense. Moving forward, spatial resolution and miniaturization are

required to be further improved in order to incorporate into robots or even humans with the help of advanced photolithographic technologies. The smart chips integrating sensing modules, LEDs, image analysis modules, and wireless transmitters/receivers make them “smarter” and help us to find more potential applications in robotics, prosthetics, healthcare, human-machine interface, and intelligent industry.

Experimental Section

Fabrication of a tactile perception smart finger The basic structure of the smart finger is composed of a single ion conducting electrolyte sandwiched by gold and aluminum electrodes. A 100 nm gold layer was deposited on a piece of 2 cm×2 cm Nafion NR-211 membrane (Dupont De Nemours) electrolyte with a thickness of 25 μm using a thermal evaporator (Beijing Technol. Science Co., LTD ZHD-300M2). An aluminum foil was used as the counter electrode. For the construction of the 5 × 5 sensory array, a 100-nm-metal layer (i.e. gold or aluminum) was first coated on the oxygen plasma-treated PET substrate being covered by a stainless-steel mask to create a customized pixel pattern. The Nafion 211 film was attached to gold electrode by pressing under 10 kPa overnight at RH 50%. Then PDMS pieces with a thickness of 2 mm and a diameter of 3 mm were sandwiched between the two electrodes to serve as the spacers. Each pixel was circular-shaped with a diameter of 9 mm and a center-to-center distance of 15.5 mm.

Characterizations The periodic stress was applied to the smart finger by using a pushing tester (Junil Tech. JIPT-120) accommodated in a digitalized humidity controller (Terra Universal 1911-24D). An oscilloscope (Agilent DSO-X-2014A) equipped with a preamplifier (SRS SR-570) was used for voltage and current measurements throughout this research. The weight change of the Nafion film after moisture uptake was measured using semi-microbalance (Sartorius Cubis(R) II

MCA125S-2S00-I). The ionic conductivity of Nafion film was determined using Admiral Squidstat Plus potentiostat with impedance spectroscopy capability, over the frequency range from 0.1 Hz to 1 MHz. The blocking stainless-steel electrodes were used to be assembled the symmetric electrode/electrolyte/electrode cells. All tests were conducted at 25 ± 2 ℃. The surface morphology of the Nafion film before and after long-term operation were investigated using a field-emission scanning electron microscope (Hitachi S4800-7952).

Image analysis application software for self-powered smart finger The LED is directly connected to the smart finger to obtain the separation TE signal from the electrical outputs individually. The LED was positioned in the dark chamber with optical opening where a Android smartphone (Samsung Galaxy Note 10+) was mounted to take a video of LED lightning. A home-built image analysis system was developed for the quantitative characterization of LED brightness, which is termed 'Smart Color Analysis System (SCAS)'. The SCAS is an Android application software built using Android Studio. This application has been built to systematically extract the RGB components from the snapshot of the video, followed by perceived brightness. The SCAS workflow is detailed as follows:

Image loading The user can load the snapshot image of LED lighting for the RGB components extraction.

Image preprocessing Once the user loads the snapshot image to be analyzed, it can be resized and cropped to remove the background.

Image analysis The truncated image is converted into a matrix containing the RGB and brightness values of each pixel. The brightness was estimated by the equation $B = \sqrt{0.299\,R^2 + 0.587\,G^2 + 0.114\,B^2}$ [45] where R, G, B indicate the values of RGB color

components in 0 to 255 scales, respectively. The matrix is processed to find the most frequent color from all pixels over the image selected. First, the occurrence of individual RGB components is counted and sorted in descending order. We chose six color matrices being the most frequently observed in the image by sorting them in the orders of RGB, RBG, GRB, GBR, BGR, and BRG. The most bright color components are selected as a representative color of the image. In this software, the pixels featuring a brightness of > 15 are analyzed to filter the black background.

Tactile perception using machine learning The supervised machine learning was employed to predict the pressure, vibration, and humidity from responses of the smart finger using a MATLAB programming language (Mathworks Inc., Natick, MA). For the classification of individual RH, pressure, and frequency, the 'patternnet' algorithmm was employed to train the neural network in which the preprocessed data was split into 70:15:15 by percent for training, validation, and testing. In order to quantitatively predict the RH, pressure, and frequency values from the brightness and output voltage, two pre-trained models were developed to train the network by the 'fitnet' algorithm: Brightness/contact HE and contact HE/separation TE/RH/pressure/frequency. With two models, the web app with user interface was constructed to real-time analysis of smart skin signals. Once the user inputs the brightness and separation TE value into the web app, the contact HE value will be estimated from the pre-trained model, and then RH, pressure, and freqeuncy are predicted from contact HE and separation TE signals.

Author contributions

D.-M.S. conceived the overall research goals and aims. D.-M.S. and X.M. designed the experiments. X.M. fabricated devices and performed the characterization with help from E.K., J.Z., J.G., X.H. and J.T.K. E.K developed the mobile app. D.-M.S. developed both classification and

regression models using machine learning with help from C.K. D.-M.S. developed the web-based server. X.M. and D.-M.S. performed the data analysis and organized the results. X.M. and E.K composed the layout of the Supplementary Videos and D.-M.S. created the videos. All the authors contributed to writing the manuscript.

Competing interests

The authors declare the following competing interests: the University of Hong Kong has applied for a patent (US application no. 63/453,817) on some of the technology discussed herein, on which X.M., E.K., J.Z., J.G. and D.-M. S. are listed as co-inventors.

Additional information

Supplementary information The online version contains supplementary material available at .

Data availability

The data in this study are available within the paper and its Supplementary Information.

Acknowledgements

The authors acknowledge the financial support of the Early Career Scheme of the Research Grants Council of the Hong Kong Special Administrative Region, China, under Award Number 27202920.

Figures

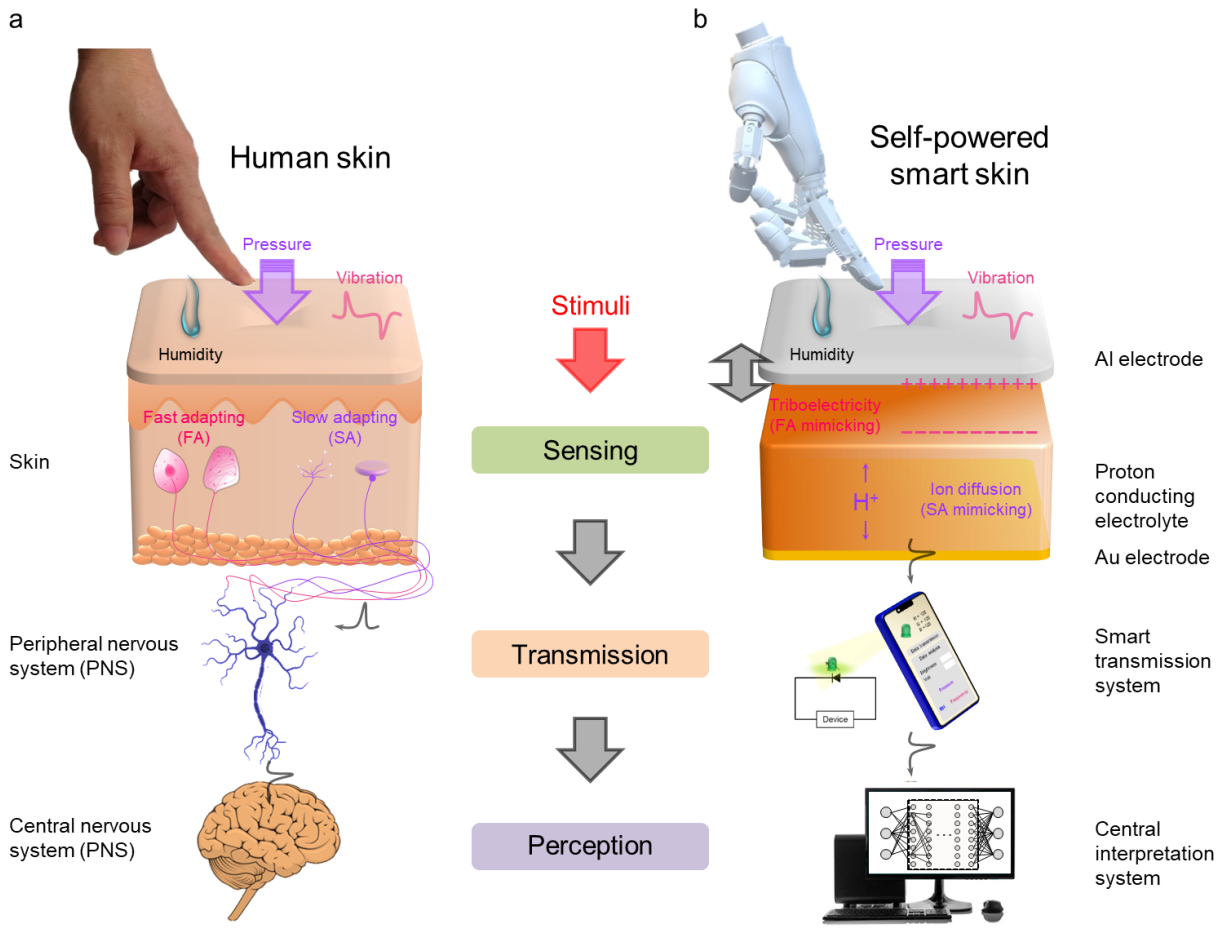

Figure 1 | Self-powered smart skin system for multimodal tactile perception. a, Illustration of tactile perception over the course of the human skin and nervous system. The tactile stimuli, such as pressure, vibration, heat, and humidity, are encoded into the electrical signal by mechano- and thermoreceptors. The signals are transmitted to the nervous systems for identification and interpretation. **b**, Schematics of tactile perception in a self-powered smart skin. The tactile stimuli are sensed in the forms of triboelectric and hygroelectric signals by the smart skin module comprising a single-ion conducting electrolyte and two electrodes. The identification and interpretation of signals being transmitted by the handheld device are performed in the central computer equipped with machine learning.

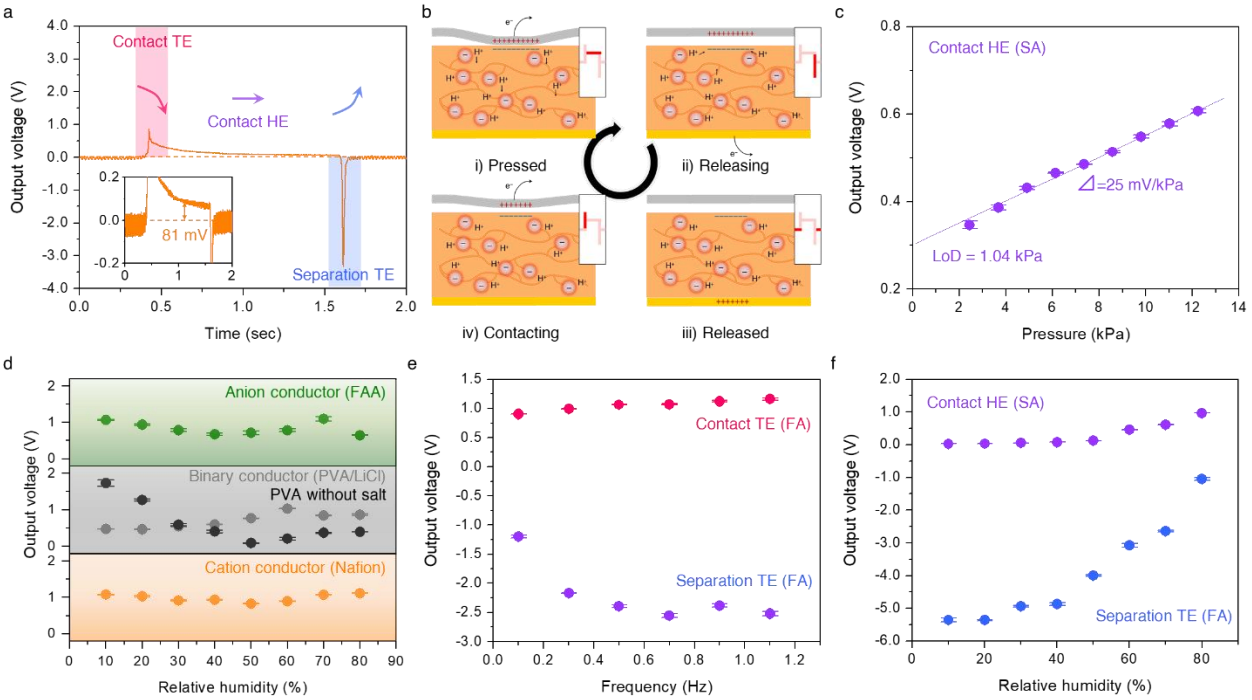

Figure 2 | Tactile sensation using a smart finger. a, The voltage output of the smart finger under the stimuli of 50 % RH, 4.90 kPa with 0.3 Hz. **b**, Schematic illustration of the working principle. **c**, The pressure sensitivity of hygroelectric output voltages. **d**, Contact electrification outputs of the smart finger featuring anion conducting (green), cation conducting (orange), dual-ions conducting (grey), and non-conducting (black) electrolytes as changing RHs. The presence of mobile ions in the electrolyte yields the constant contact TE peaks. **e**, Triboelectric output voltages with increasing frequency. **f**, Humidity sensing capability of the smart finger.

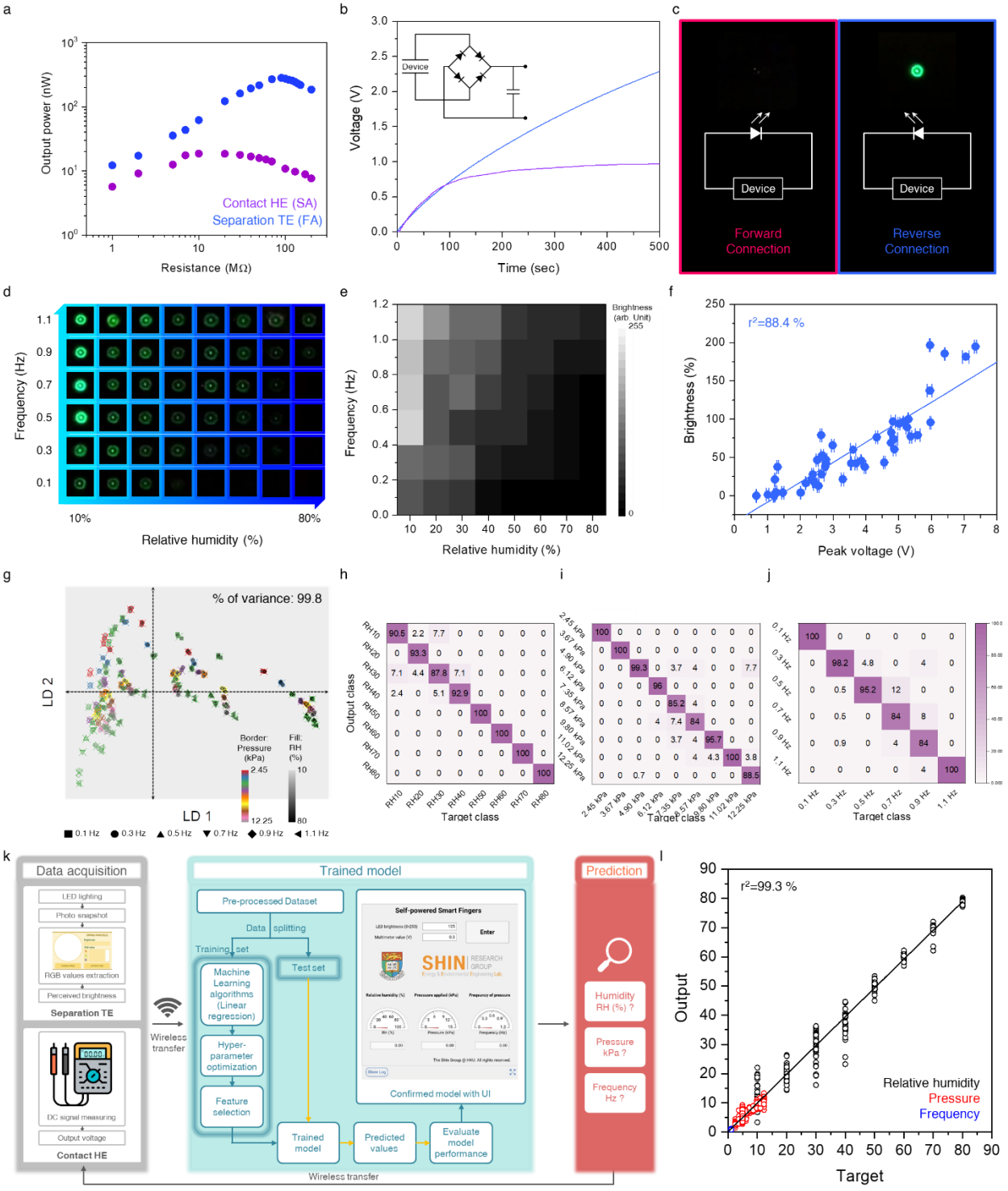

Figure 3 | Self-powered tactile perception with machine learning. a, Output powers depending on the load resistance for contact hygroelectric and separation triboelectric signals. **b**, Capacitive charging with individual contact hygroelectric and separation triboelectric signals. The inset indicates an equivalent circuit

for capacitive charging. **c**, Lightening of a LED with forward (red) and reverse (blue) connections. **d**, The snapshots of LED lighting with varying RHs and frequencies. **e**, The perceived brightness corresponding to the images in d using home-built image analysis application. **f**, Comparison of separation TE peak voltage and brightness calculated. Solid lines are the linear fit. **g**, Discrimination capability of the smart finger. LD1 and LD2 represent the first linear discriminant factor and second linear discriminant factor, respectively. **h−j**, Confusion map of the machine learning results for 8 humid, 9 pressure, and 6 vibrational conditions, respectively. **k**, Flow diagram of tactile perception from sensation to interpretation. **l**, Regression plot of the machine learning results of pre-trained model.

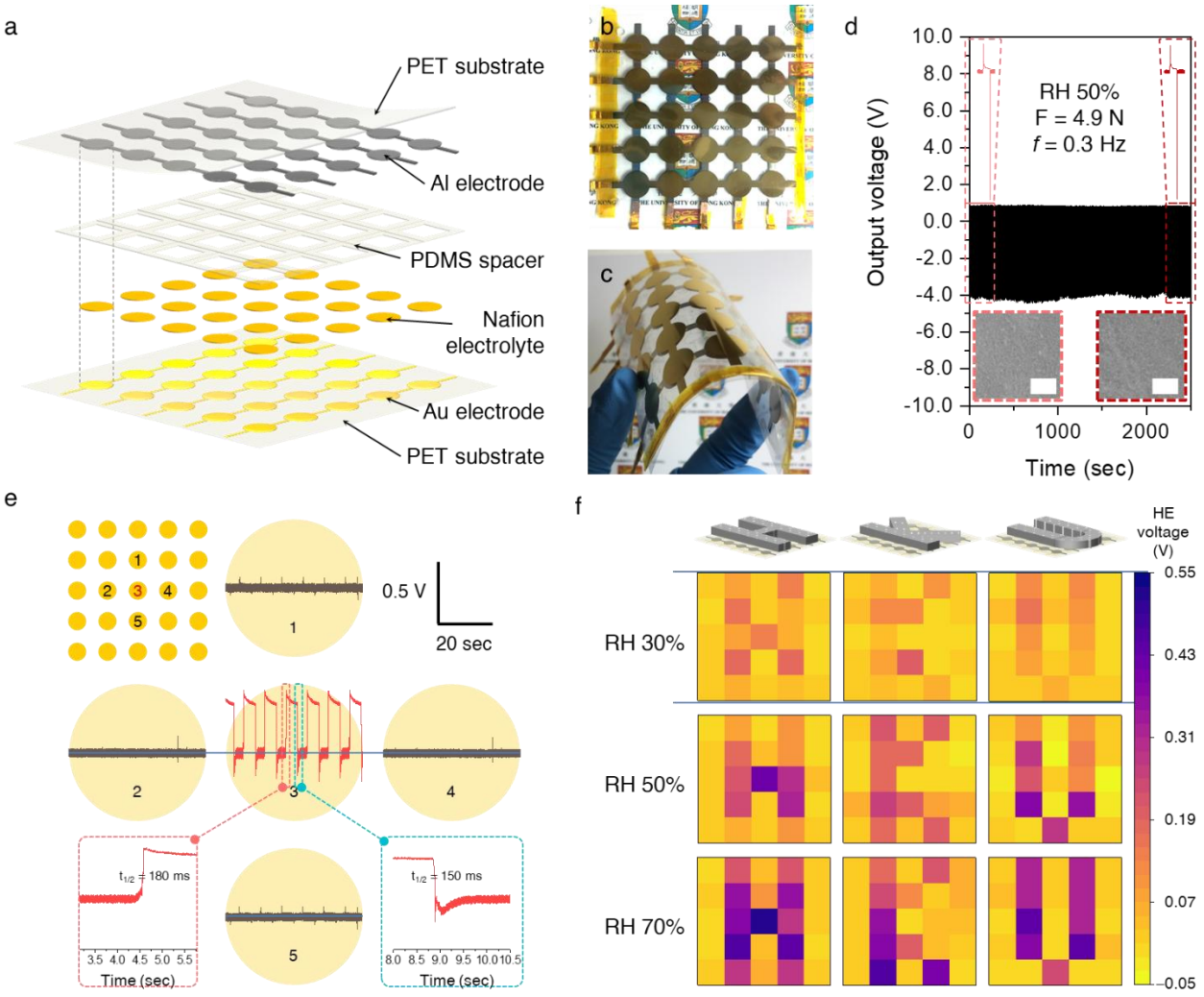

Figure 4 | Tactile perception mapping. a, Schematic of a multiarray smart skin featuring the set of 5 x 5 electrodes and a single ion conducting electrolyte. **b**, The photograph of the multiarray smart skin fabricated. **c**, The flexibility of the smart skin. **d**, The robustness and durability of the smart skins over 5000 cycles. Inset images display the morphologies of the electrolyte before and after cycling, respectively. Scale bar = 250 nm. **e**, Crosstalk between neighbouring pixels and the response/relaxation time of the smart skin. **f**, Tactile perception mapping of the smart skin at the different RHs while being pressed with the convex character patterns of 'HKU'.

References

1. Lumpkin, E.A. & Caterina, M.J. Mechanisms of sensory transduction in the skin. *Nature* **445**, 858-865 (2007).
2. Filingeri, D. & Havenith, G. Human skin wetness perception: psychophysical and neurophysiological bases. *Temperature* **2**, 86-104 (2015).
3. Chen, T. *et al.* Triboelectric Self-Powered Wearable Flexible Patch as 3D Motion Control Interface for Robotic Manipulator. *ACS Nano* **12**, 11561-11571 (2018).
4. Jin, T. *et al.* Triboelectric nanogenerator sensors for soft robotics aiming at digital twin applications. *Nat. Commun.* **11**, 5381 (2020).
5. Sun, Z. *et al.* Artificial Intelligence of Things (AIoT) Enabled Virtual Shop Applications Using Self-Powered Sensor Enhanced Soft Robotic Manipulator. *Adv. Sci.* **8**, 2100230 (2021).
6. Kim, J. *et al.* Stretchable silicon nanoribbon electronics for skin prosthesis. *Nat. Commun.* **5**, 5747 (2014).
7. Wang, S. *et al.* Skin electronics from scalable fabrication of an intrinsically stretchable transistor array. *Nature* **555**, 83-88 (2018).
8. Hammock, M.L., Chortos, A., Tee, B.C.K., Tok, J.B.H. & Bao, Z. 25th Anniversary Article: The Evolution of Electronic Skin (E-Skin): A Brief History, Design Considerations, and Recent Progress. *Adv. Mater.* **25**, 5997-6038 (2013).
9. Beker, L. *et al.* A bioinspired stretchable membrane-based compliance sensor. *PNAS* **117**, 11314-11320 (2020).
10. Park, J., Kim, M., Lee, Y., Lee, H.S. & Ko, H. Fingertip skin–inspired microstructured ferroelectric skins discriminate static/dynamic pressure and temperature stimuli. *Sci. Adv.* **1**, e1500661 (2015).
11. Zhang, F., Zang, Y., Huang, D., Di, C.-a. & Zhu, D. Flexible and self-powered temperature–pressure dual-parameter sensors using microstructure-frame-supported organic thermoelectric materials. *Nat. Commun.* **6**, 8356 (2015).
12. Yang, J. *et al.* Flexible Smart Noncontact Control Systems with Ultrasensitive Humidity Sensors. *Small* **15**, 1902801 (2019).
13. Tolvanen, J., Hannu, J. & Jantunen, H. Hybrid Foam Pressure Sensor Utilizing Piezoresistive and Capacitive Sensing Mechanisms. *IEEE Sens. J.* **17**, 4735-4746 (2017).
14. Wei, Q. *et al.* MXene-Sponge Based High-Performance Piezoresistive Sensor for Wearable Biomonitoring and Real-Time Tactile Sensing. *Small Methods* **6**, 2101051 (2022).
15. Narita, F. *et al.* A Review of Piezoelectric and Magnetostrictive Biosensor Materials for Detection of COVID-19 and Other Viruses. *Adv. Mater.* **33**, 2005448 (2021).

16. Kim, Y.-G., Song, J.-H., Hong, S. & Ahn, S.-H. Piezoelectric strain sensor with high sensitivity and high stretchability based on kirigami design cutting. *npj Flexible Electron.* **6**, 52 (2022).

17. Mannsfeld, S.C.B. *et al.* Highly sensitive flexible pressure sensors with microstructured rubber dielectric layers. *Nat. Mater.* **9**, 859-864 (2010).

18. Xie, M. *et al.* Flexible Multifunctional Sensors for Wearable and Robotic Applications. *Adv. Mater. Technol.* **4**, 1800626 (2019).

19. Shin, Y.-E. *et al.* Self-powered triboelectric/pyroelectric multimodal sensors with enhanced performances and decoupled multiple stimuli. *Nano Energy* **72**, 104671 (2020).

20. Gong, S. *et al.* A wearable and highly sensitive pressure sensor with ultrathin gold nanowires. *Nat. Commun.* **5**, 3132 (2014).

21. Zhu, B. *et al.* Microstructured Graphene Arrays for Highly Sensitive Flexible Tactile Sensors. *Small* **10**, 3625-3631 (2014).

22. Chen, X. *et al.* A chaotic pendulum triboelectric-electromagnetic hybridized nanogenerator for wave energy scavenging and self-powered wireless sensing system. *Nano Energy* **69**, 104440 (2020).

23. Li, X. *et al.* Networks of High Performance Triboelectric Nanogenerators Based on Liquid–Solid Interface Contact Electrification for Harvesting Low-Frequency Blue Energy. *Adv. Energy Mater.* **8**, 1800705 (2018).

24. Jeong, J. *et al.* A Sustainable and Flexible Microbrush-Faced Triboelectric Generator for Portable/Wearable Applications. *Adv. Mater.* **33**, 2102530 (2021).

25. Amangeldinova, Y. *et al.* Enhancing Electrical Outputs of Piezoelectric Nanogenerators by Controlling the Dielectric Constant of ZnO/PDMS Composite. *Micromachines* **12** (2021).

26. Phan, H. *et al.* Aerodynamic and aeroelastic flutters driven triboelectric nanogenerators for harvesting broadband airflow energy. *Nano Energy* **33**, 476-484 (2017).

27. Meng, K. *et al.* Flexible Weaving Constructed Self-Powered Pressure Sensor Enabling Continuous Diagnosis of Cardiovascular Disease and Measurement of Cuffless Blood Pressure. *Adv. Funct. Mater.* **29**, 1806388 (2019).

28. Zhao, L. *et al.* Reversible Conversion between Schottky and Ohmic Contacts for Highly Sensitive, Multifunctional Biosensors. *Adv. Funct. Mater.* **30**, 1907999 (2020).

29. Ma, Y. *et al.* Self-Powered, One-Stop, and Multifunctional Implantable Triboelectric Active Sensor for Real-Time Biomedical Monitoring. *Nano Lett.* **16**, 6042-6051 (2016).

30. Sun, J., Yang, A., Zhao, C., Liu, F. & Li, Z. Recent progress of nanogenerators acting as biomedical sensors in vivo. *Sci. Bull.* **64**, 1336-1347 (2019).

31. Wu, C., Wang, A.C., Ding, W., Guo, H. & Wang, Z.L. Triboelectric Nanogenerator: A Foundation of the Energy for the New Era. *Adv. Energy Mater.* **9**, 1802906 (2019).

32. Wang, Z.L. Triboelectric Nanogenerator (TENG)—Sparking an Energy and Sensor Revolution. *Adv. Energy Mater.* **10**, 2000137 (2020).

33. Abraira, Victoria E. & Ginty, David D. The Sensory Neurons of Touch. *Neuron* **79**, 618-639 (2013).

34. Wang, M. *et al.* Artificial Skin Perception. *Adv. Mater.* **33**, 2003014 (2021).

35. Chun, S. *et al.* Self-Powered Pressure- and Vibration-Sensitive Tactile Sensors for Learning Technique-Based Neural Finger Skin. *Nano Lett.* **19**, 3305-3312 (2019).

36. Lee, Y. *et al.* Flexible Pyroresistive Graphene Composites for Artificial Thermosensation Differentiating Materials and Solvent Types. *ACS Nano* **16**, 1208-1219 (2022).

37. Huang, Y. *et al.* Interface-mediated hygroelectric generator with an output voltage approaching 1.5 volts. *Nat. Commun.* **9**, 4166 (2018).

38. Liu, X. *et al.* Power generation from ambient humidity using protein nanowires. *Nature* **578**, 550-554 (2020).

39. Chun, S., Kim, Y., Jung, H. & Park, W. A flexible graphene touch sensor in the general human touch range. *Appl. Phys. Lett.* **105**, 041907 (2014).

40. Németh, E., Albrecht, V., Schubert, G. & Simon, F. Polymer tribo-electric charging: dependence on thermodynamic surface properties and relative humidity. *J. Electrostat.* **58**, 3-16 (2003).

41. Nguyen, V. & Yang, R. Effect of humidity and pressure on the triboelectric nanogenerator. *Nano Energy* **2**, 604-608 (2013).

42. Fan, F.-R., Tian, Z.-Q. & Lin Wang, Z. Flexible triboelectric generator. *Nano Energy* **1**, 328-334 (2012).

43. Shin, D.-M. *et al.* A Single-Ion Conducting Borate Network Polymer as a Viable Quasi-Solid Electrolyte for Lithium Metal Batteries. *Adv. Mater.* **32**, 1905771 (2020).

44. Paren, B.A. *et al.* Superionic Li-Ion Transport in a Single-Ion Conducting Polymer Blend Electrolyte. *Macromolecules* **55**, 4692-4702 (2022).

45. Finley, D.R. HSP Color Model — Alternative to HSV (HSB) and HSL. *https://alienryderflex.com/hsp.html* (2006).

46. Zhou, Z. *et al.* Sign-to-speech translation using machine-learning-assisted stretchable sensor arrays. *Nat. Electron.* **3**, 571-578 (2020).

47. Qu, X. *et al.* Artificial tactile perception smart finger for material identification based on triboelectric sensing. *Sci. Adv.* **8**, eabq2521 (2022).

48. Pyo, S., Lee, J., Bae, K., Sim, S. & Kim, J. Recent Progress in Flexible Tactile Sensors for Human-Interactive Systems: From Sensors to Advanced Applications. *Adv. Mater.* **33**, 2005902 (2021).

49. Kang, S. *et al.* Highly Sensitive Pressure Sensor Based on Bioinspired Porous Structure for Real-Time Tactile Sensing. *Adv. Electron. Mater.* **2** (2016).

Supplementary Information

Table of Contents

Supplementary Figures

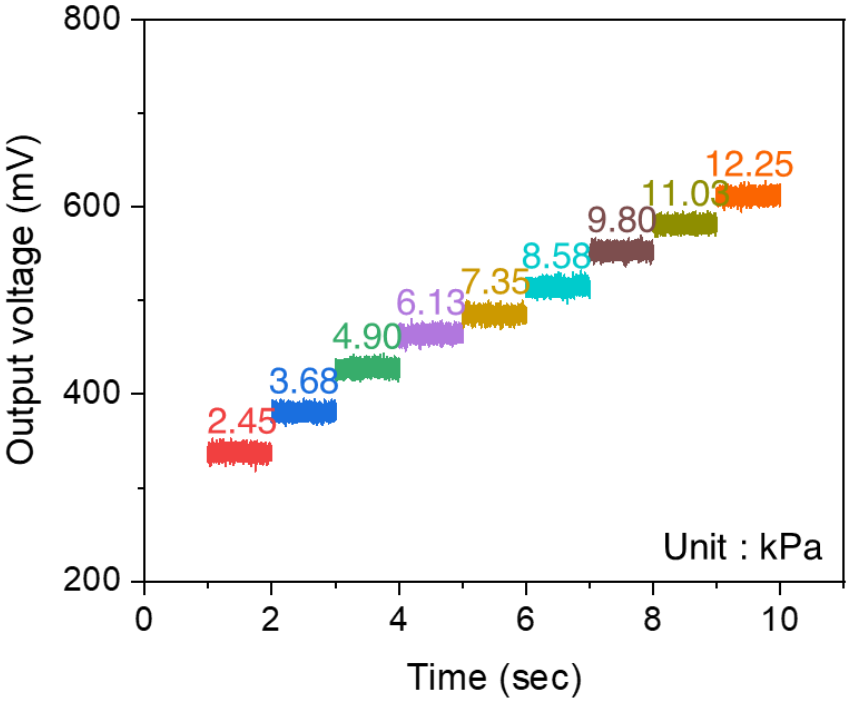

Supplementary Figure 1 | Hygroelectric output voltage of smart finger as increasing the static pressure.

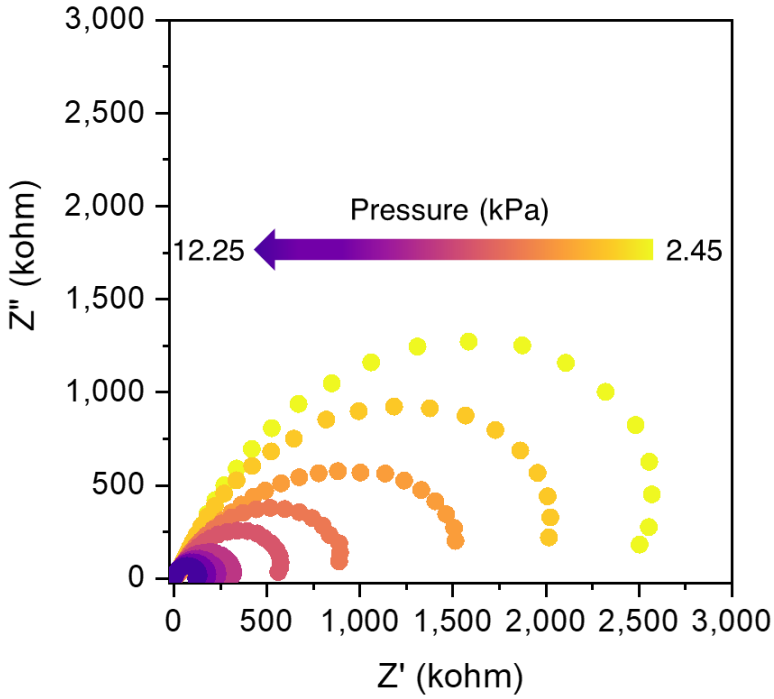

Supplementary Figure 2 | Nyquist plot of smart finger with differing pressure applied.

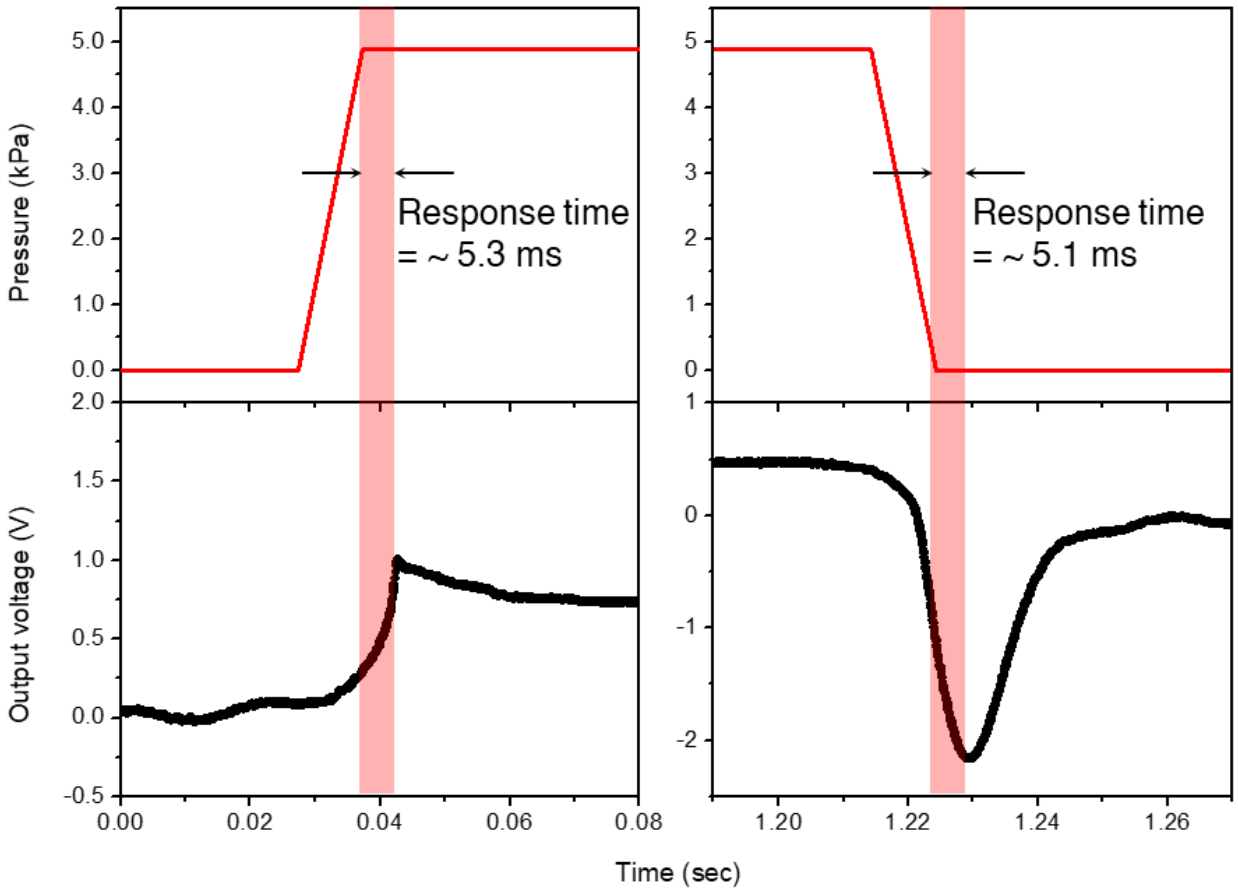

Supplementary Figure 3 | Response time for activation (left) and restoration (right) with compressing-releasing profile.

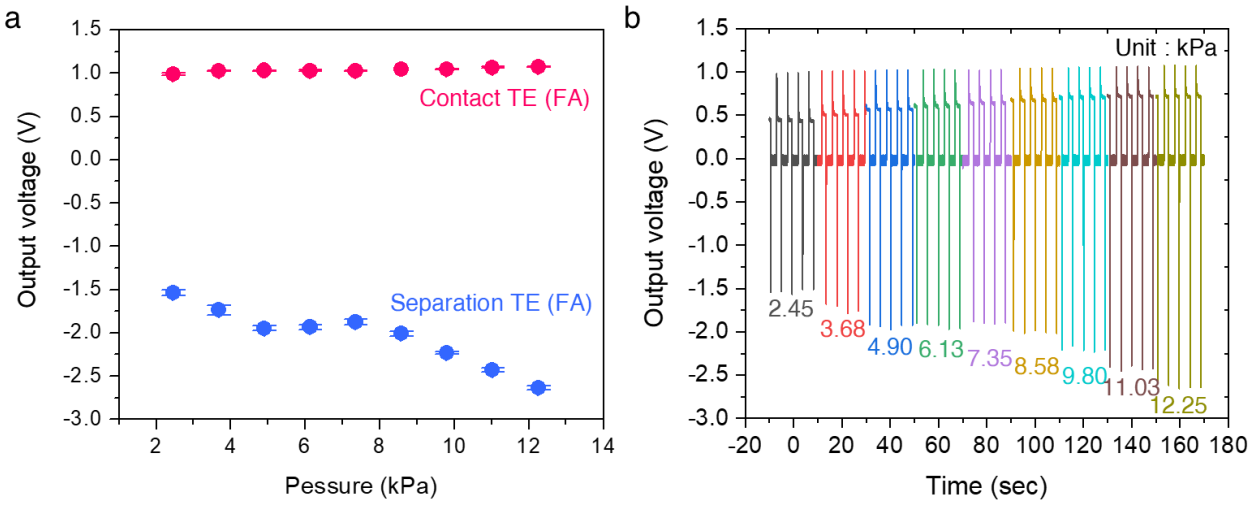

Supplementary Figure 4 | a, Output voltages of smart finger as increasing the dynamic pressure. **b**, Dynamic pressure sensitivity of triboelectric signals.

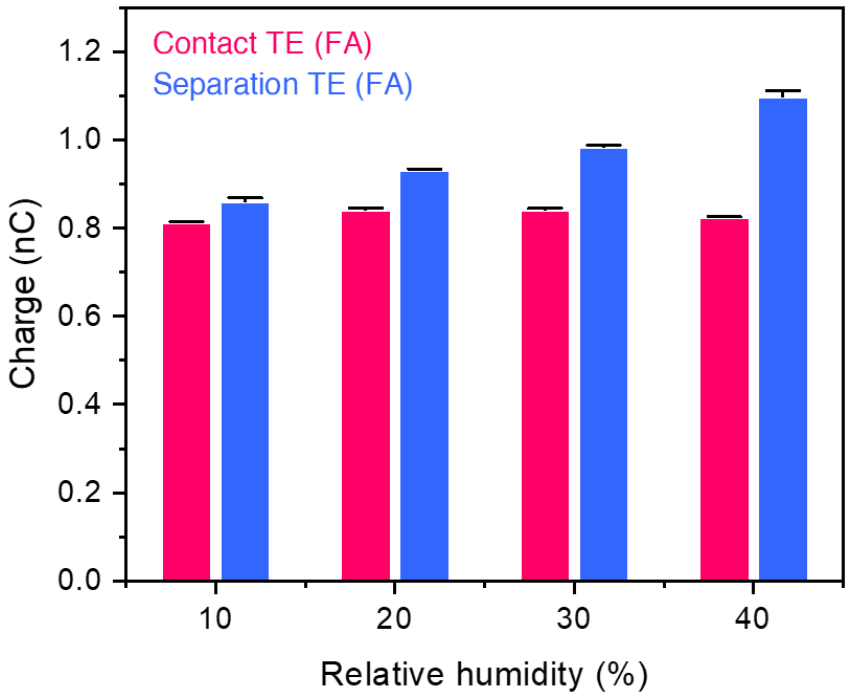

Supplementary Figure 5 | Charge accumulation driven by contact (pink) and separation (blue) triboelectric signals at different humidities.

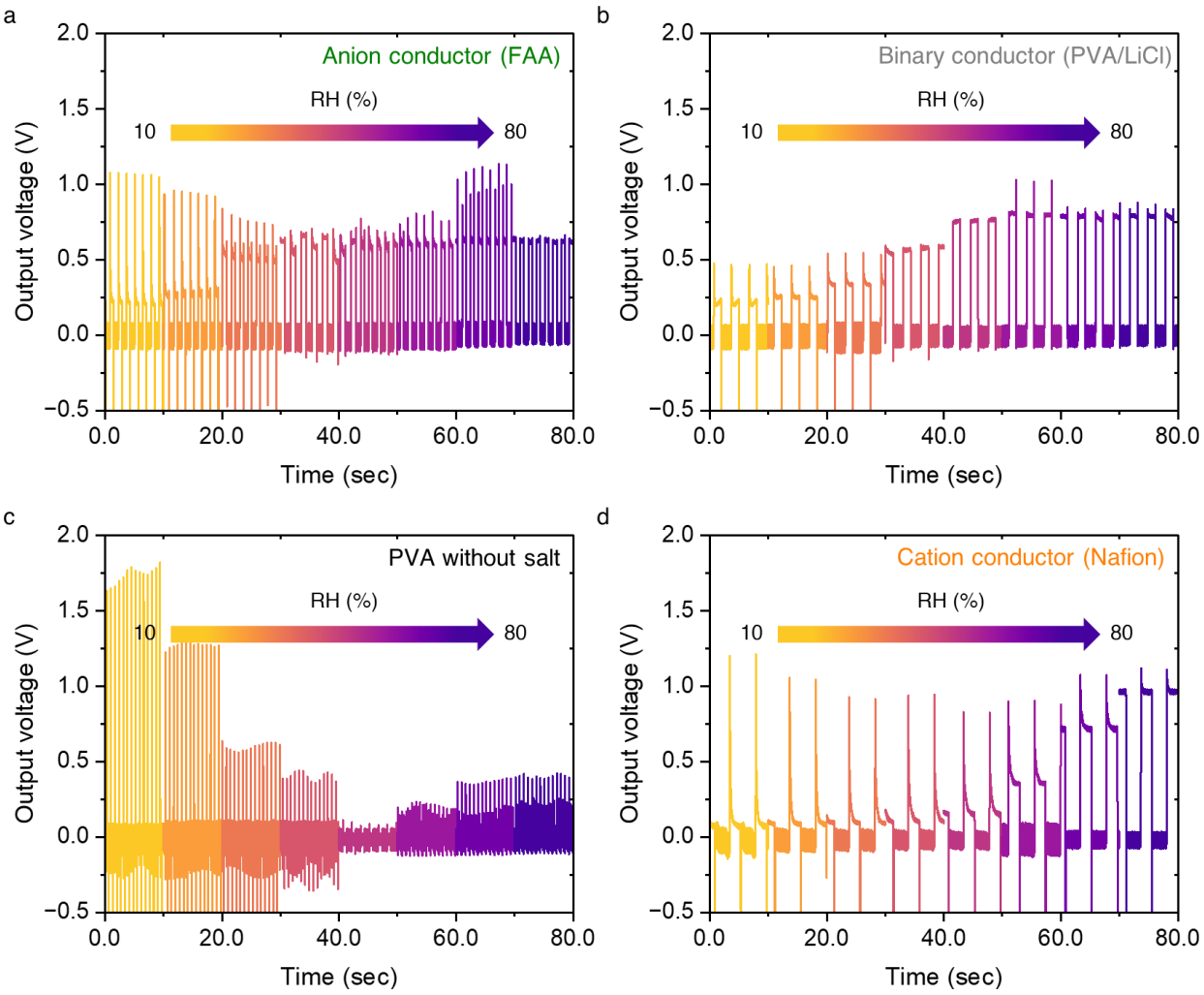

Supplementary Figure 6 | Output voltages of smart fingers comprising two electrodes and different electrolytes, including anion conductor (**a**), binary conductor (**b**), PVA without salt (**c**), and cation conductor (**d**).

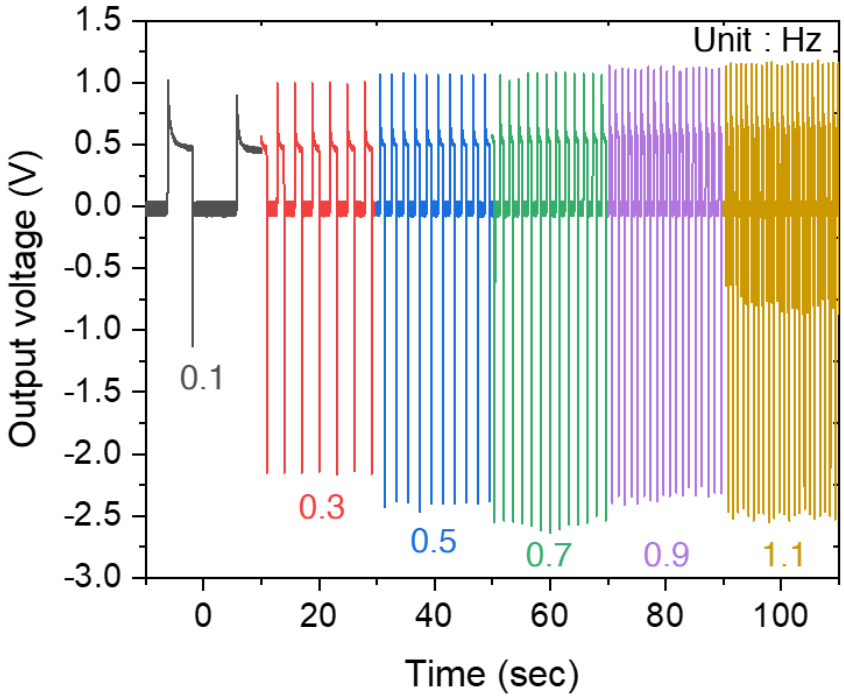

Supplementary Figure 7 | Output voltages of smart finger as increasing the frequency of dynamic pressure.

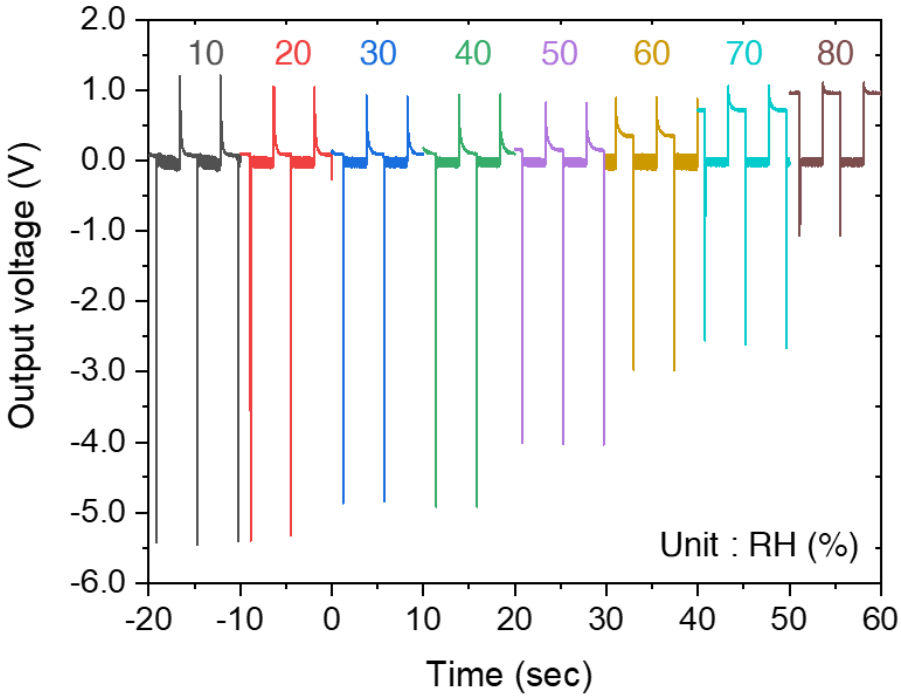

Supplementary Figure 8 | Output voltages of smart finger as increasing the RHs.

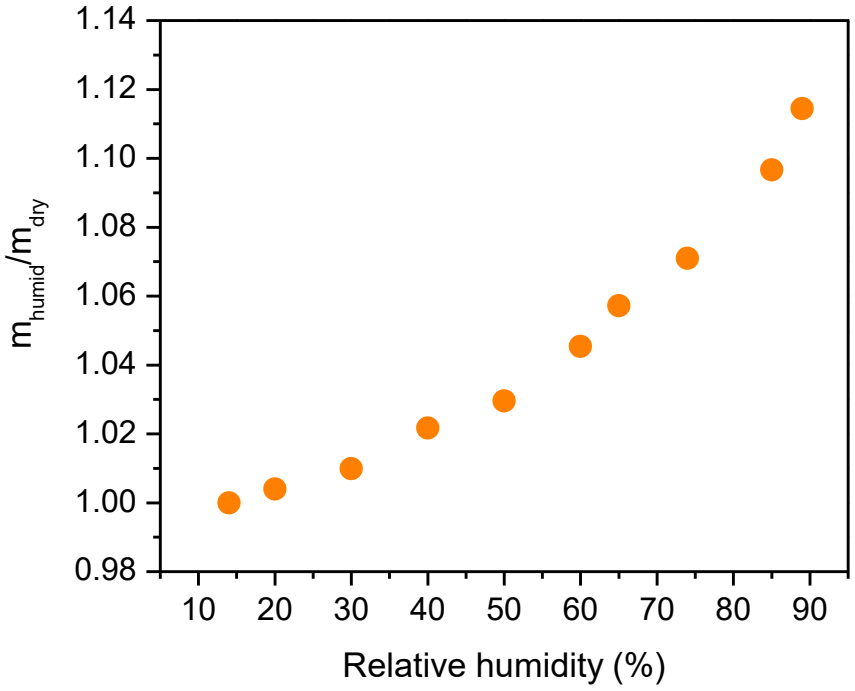

Supplementary Figure 9 | Hygroscopic property of electrolyte with RHs.

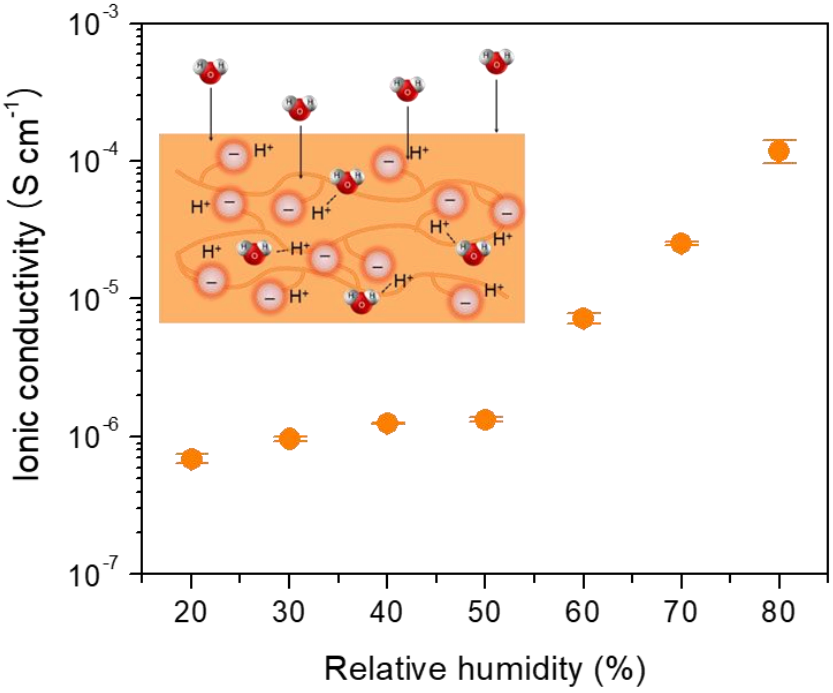

Supplementary Figure 10 | Ionic conductivity of electrolyte with RHs.

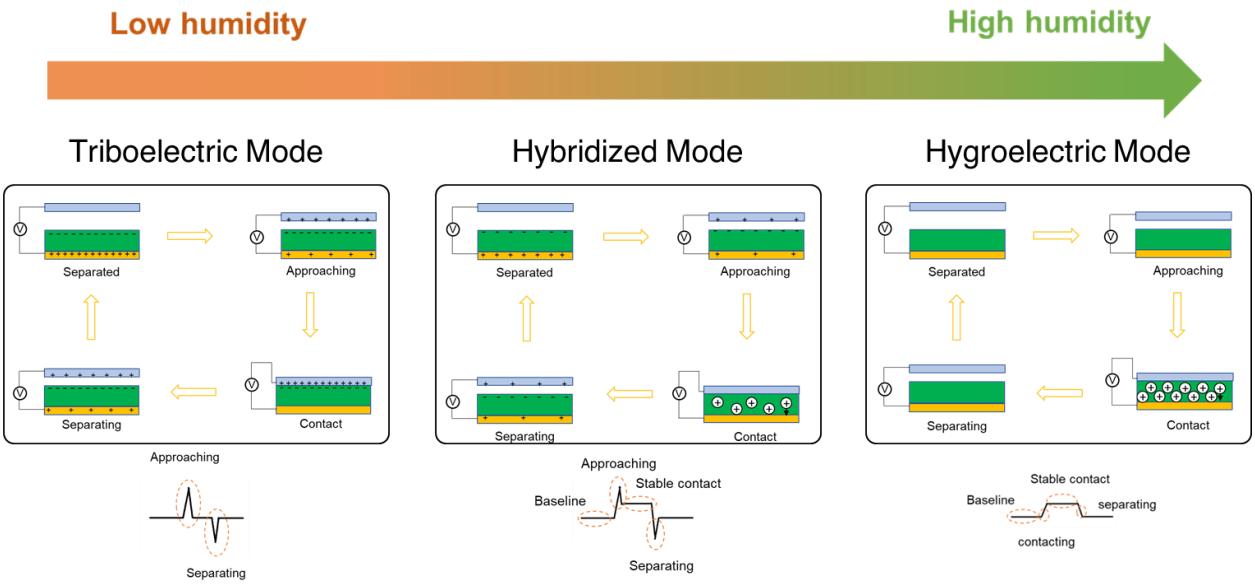

Supplementary Figure 11 | Working principle of smart finger in the broad range of humidity.

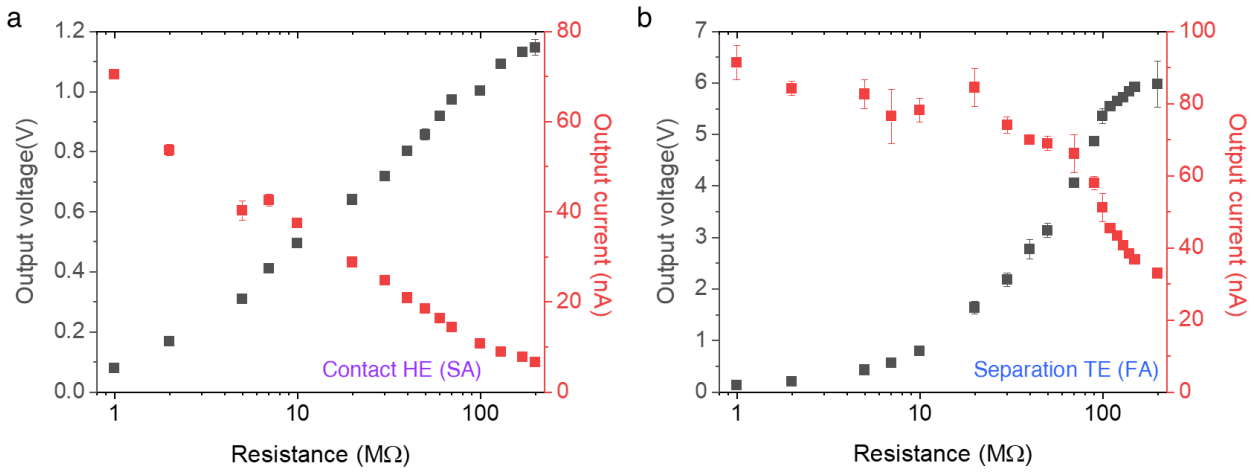

Supplementary Figure 12 | Output voltage and current of contact hygroelectric (**a**) and separation triboelectric signals (**b**) as a function of load resistance.

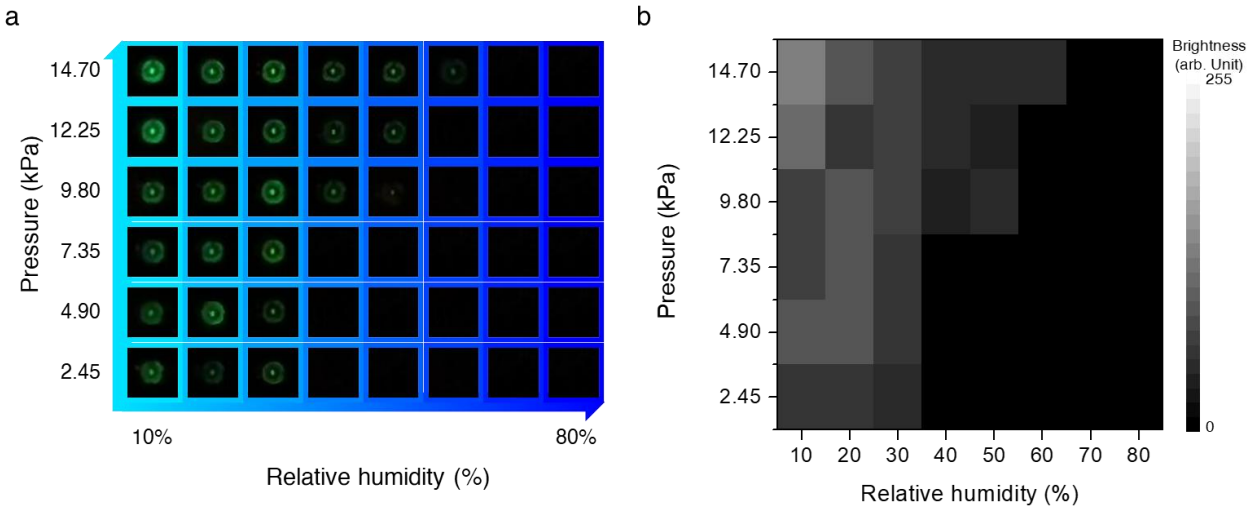

Supplementary Figure 13 | a, The snapshots of LED lighting with varying RHs and pressure. **b**, The perceived brightness corresponding to the images in d using home-built image analysis application.

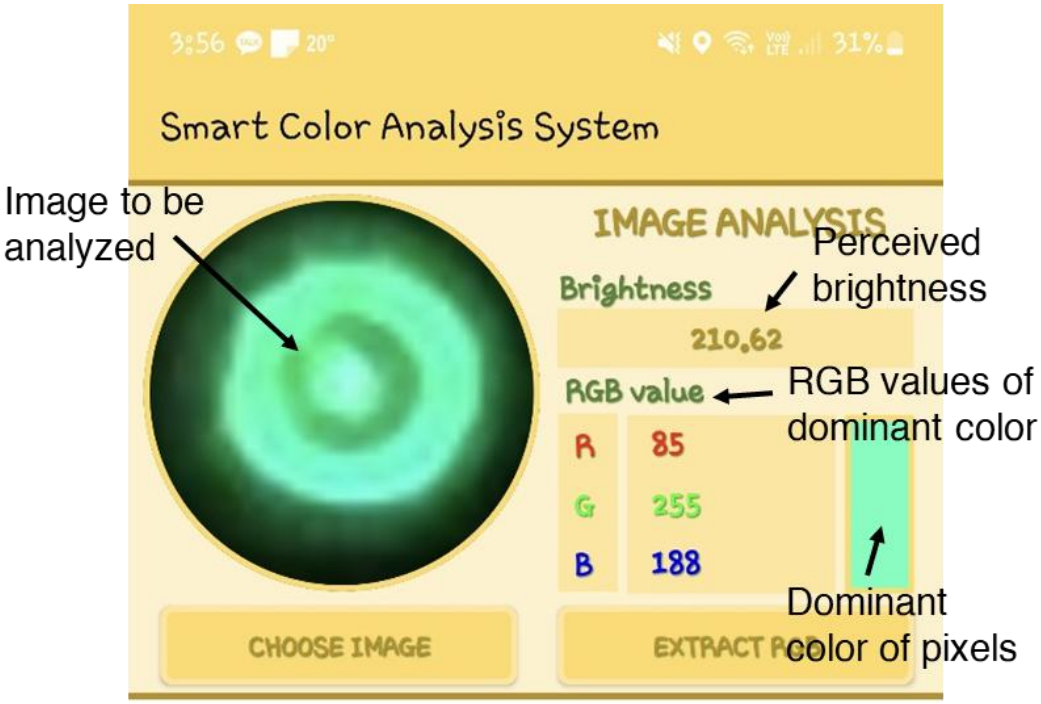

Supplementary Figure 14 | Snapshot of home-built image analysis application.

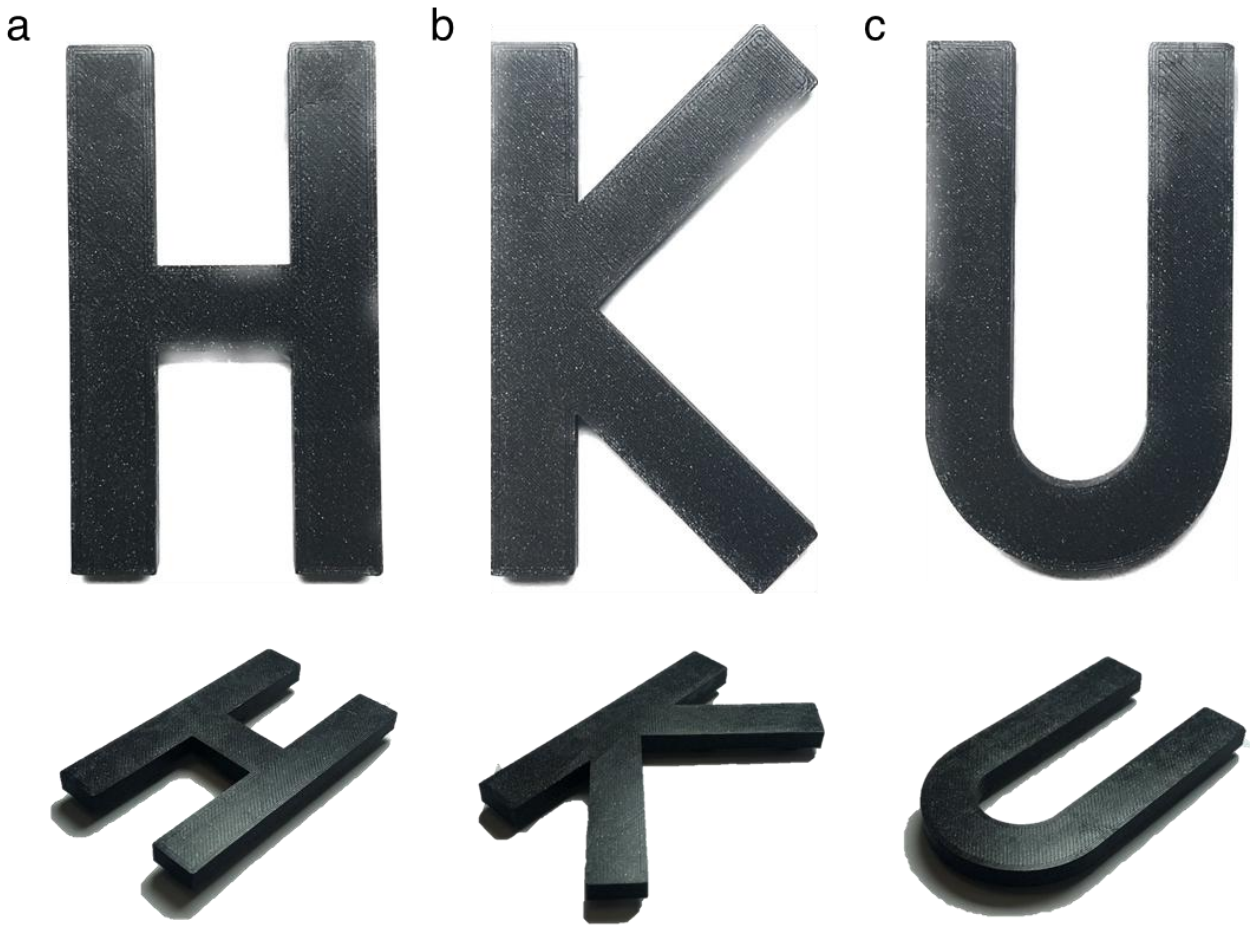

Supplementary Figure 15 | Photographs of the convex character patterns of ‘H (**a**) K (**b**) U (**c**)’.

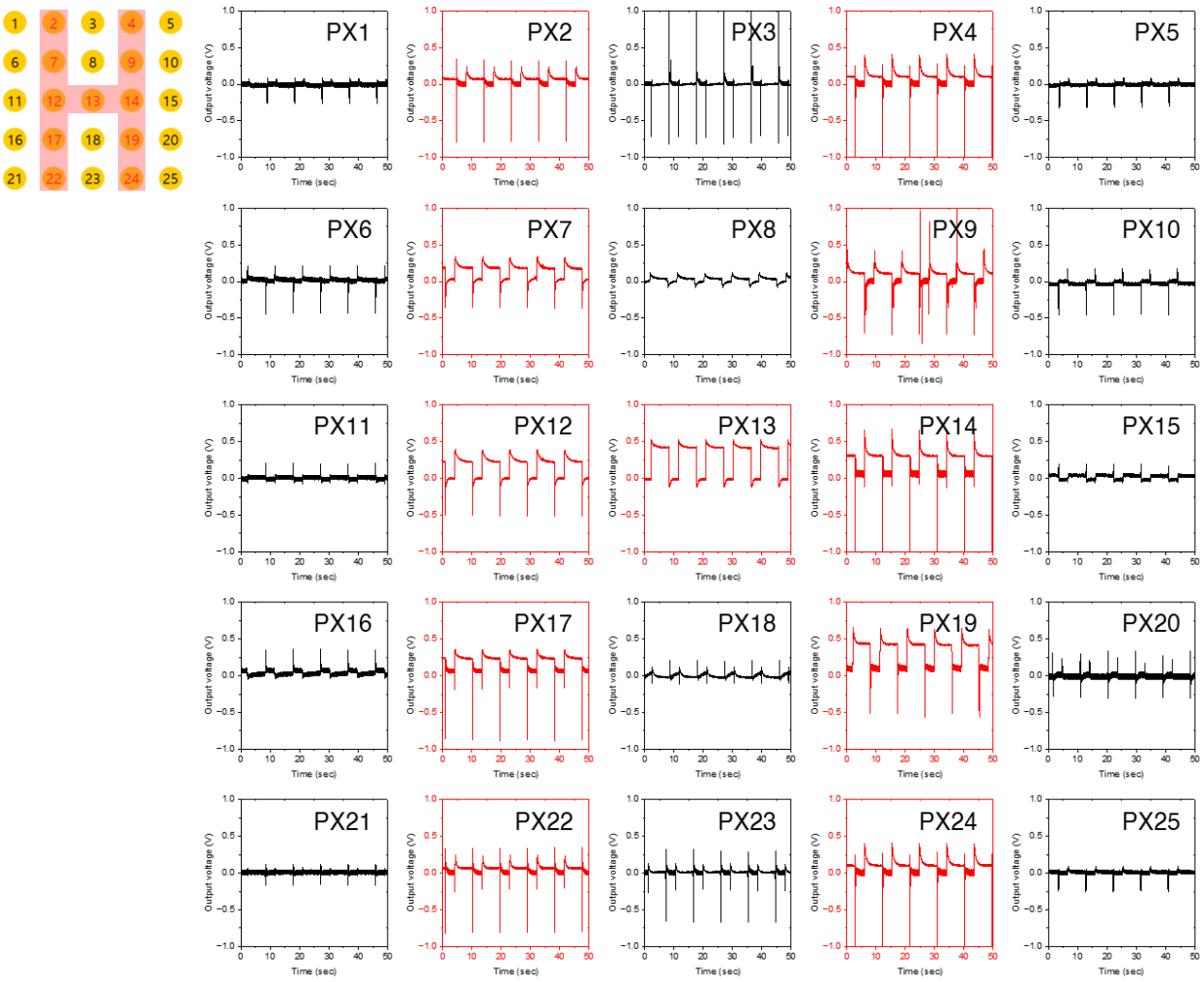

Supplementary Figure 16 | The output voltages of smart skins under the pressure with 'H' convex pattern.

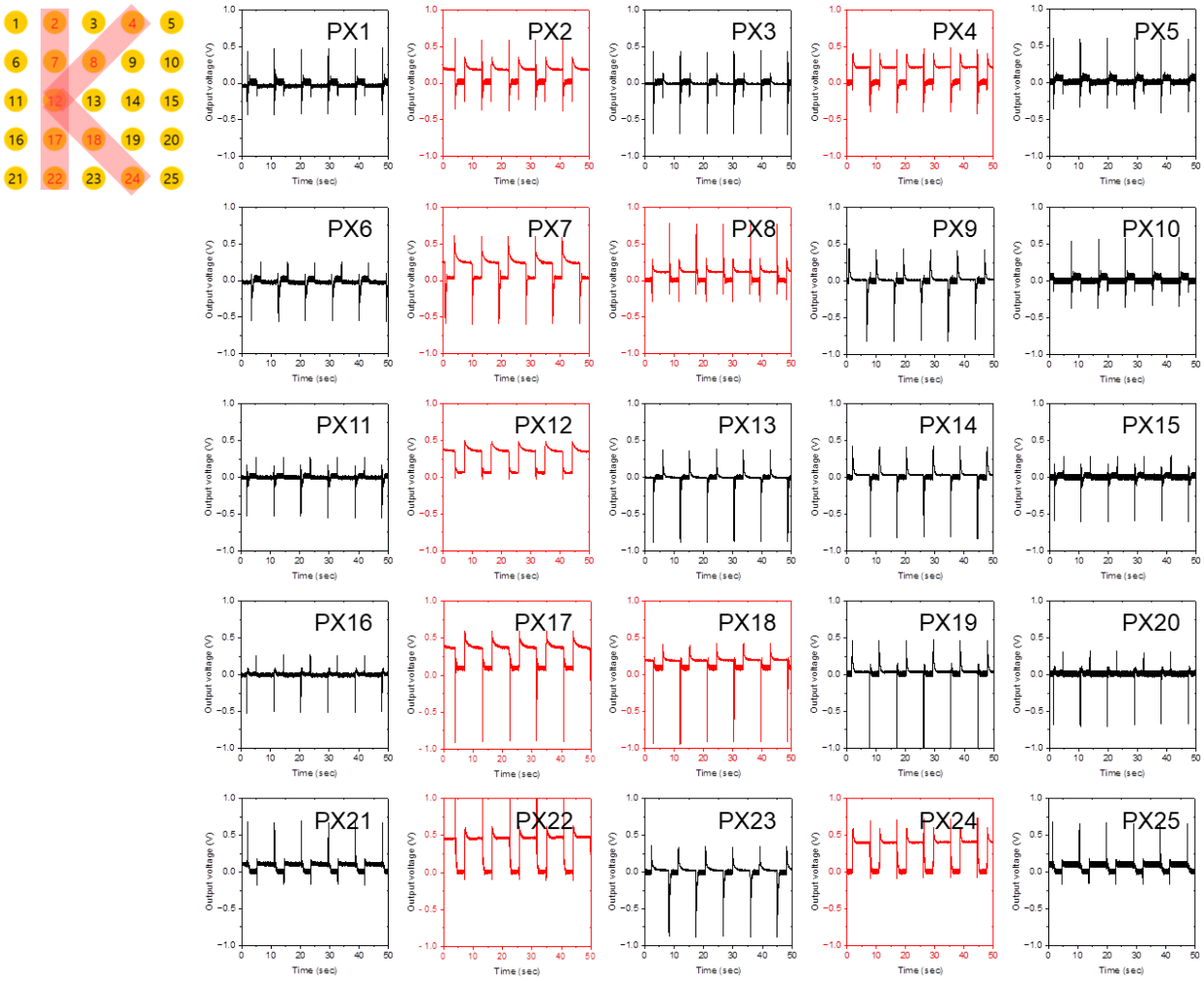

Supplementary Figure 17 | The output voltages of smart skins under the pressure with 'K' convex pattern.

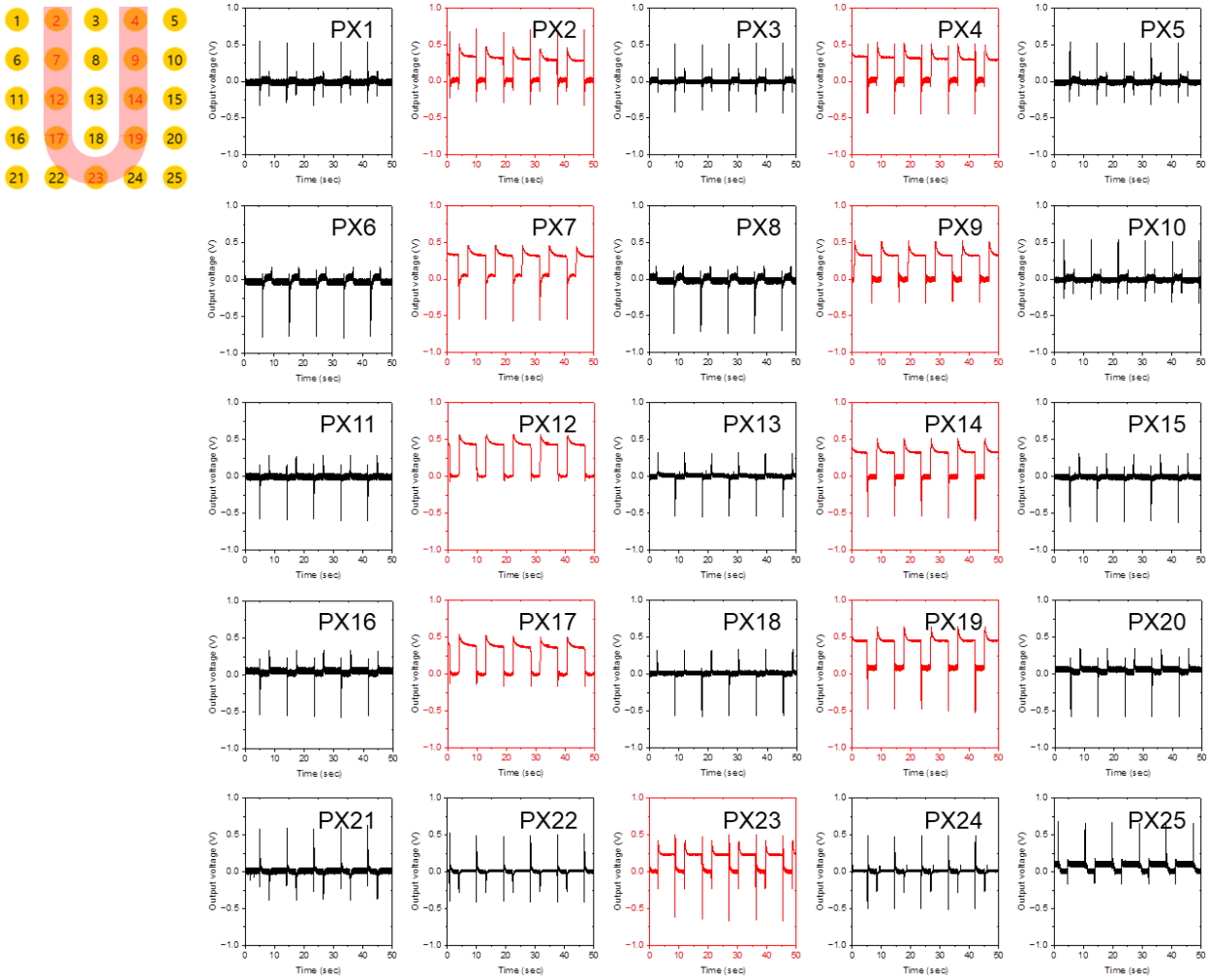

Supplementary Figure 18 | The output voltages of smart skins under the pressure with 'U' convex pattern.

Supplementary Table

Supplementary Table 1 | The current signals measured at RH50% with 4.9kPa and 0.3Hz mechanical contact and separation.

Sample No.	Conditions applied			Conditions predicted		
	RH (%)	Pressure (kPa)	Frequency (Hz)	RH (%)	Pressure (kPa)	Frequency (Hz)
1	24	4.9	0.3	29.29	5.78	0.32
2	25	6.9	0.5	28.15	7.93	0.39
3	33	8.6	0.7	32.29	9.11	0.69
4	50	6.1	1.1	64.65	7.12	1.07

Supplementary Movies

Supplementary Movie 1 | Demonstration of image analysis mobile app.

Supplementary Movie 2 | Demonstration of a web app based on the trained model.

Supplementary Movie 3 | Demonstration of self-powered smart skin system.